Magnetic indicators for evaluating plastic strains in electrical steel: Toward non-destructive assessment of the magnetic losses

S. Zhang, B. Ducharne, G. Sebald, S. Takeda, T. Uchimoto

Magnetic indicators for evaluating plastic strains in electrical steel: toward non-destructive assessment of the magnetic losses.

S. Zhang[1, 2, 4], B. Ducharne[1, 3, ✉], G. Sebald[3], S. Takeda[2], T. Uchimoto[2, 3]

1. Univ. Lyon, INSA Lyon, LGEF EA682, Villeurbanne, France
2. Institute of Fluid Science (IFS), Tohoku University, Sendai, Japan
3. ELyTMaX IRL3757, CNRS, Univ Lyon, INSA Lyon, Centrale Lyon, Université Claude Bernard Lyon 1, Tohoku University, Sendai, Japan
4. Graduate School of Engineering, Tohoku University, Sendai, Japan

✉ corresponding author: benjamin.ducharne@insa-lyon.fr

Abstract

Electric steel is widely used for magnetic conversion of electrical energy such as in electric motors and power transformers. Electric steel sheets are cut using mechanical methods (such as punching) during manufacturing. These methods induce local plastic strains, which lead to overall degradation in magnetic performance.

Plasticity and magnetic losses are physically related in electrical steel. It is impossible to measure the magnetic losses on the production line using standard methods. Non-destructive testing (NDT) based on magnetization mechanisms is a promising alternative, giving access to local plastic strains and indirectly to local magnetic losses.

In this study, a setup was designed to stimulate the magnetization mechanisms separately while maintaining the same experimental conditions. The magnetization processes related to the domain wall kinetics were revealed to be more correlated to plastic strain. The magnetic incremental permeability hysteresis area and maximal value, and the coercivity associated with Barkhausen noise were found to be the best plastic strain indicators. Additional tests in an NDT context confirmed the correlations, the equal applicability of the proposed indicators, and their viability in predicting static hysteresis loss.

Keywords

Magnetization mechanism, hysteresis cycle, magnetic incremental permeability, magnetic Barkhausen noise.

1 Introduction

Electrical steel is an iron–silicon alloy tailored to produce specific magnetic properties such as low power loss and high permeability. It is manufactured in cold-rolled strips less than 2 mm thick that are cut into laminae and stacked to form E, I, or U-shaped magnetic cores for electric transformers and motors [1]. Electrical steel may contain 0 to 6.5 wt.% silicon, but the silicon content of most commercial alloys is 3 wt.%. The silicon adjunction increases the electrical resistivity and reduces the induced eddy currents and magnetic losses [2][3].

Electrical steel can be processed without treating crystal orientation. It becomes non-oriented electrical steel (NO FeSi) and exhibits isotropic magnetic behaviors. It can also be manufactured by tightly controlling the crystal orientation relative to the lamination (Goss texture [4]) and become highly anisotropic, such as grain-oriented electrical steel (GO FeSi). NO FeSi is cheaper than GO FeSi and is preferred when cost is favored over efficiency or for applications where the magnetization direction is unknown (such as in electric motors and generators) [5].

The machining processes from the cold-rolled strip to the magnetic core induce elastic and plastic strains [6]-[12]. In the elastic region of the stress–strain curve, the magnetic properties are restored when the mechanical load is released. In the plastic region, irreversible effects are observed, including an overall degradation in magnetic properties [13].

Improved quality and optimal magnetic performances mean systematic production controls for electrical steel manufacturers [14]. However, controlling magnetic properties according to characterization standards is destructive, non-local, and incompatible with a production line's working conditions. An alternative solution consists of indirectly observing plastic strain by setting conformity thresholds and removing all unsatisfactory specimens. Local plastic strains can

be observed with X-rays or advanced imaging techniques (such as EBSD) [15][16], but their cost and complexity make them questionable in the industrial context. Ultrasound may be used to determine plastic strain [17]. Alternatively, this work proposes using magnetic signatures.

Magnetic signatures are relatively easy to observe non-destructively, and some are highly plastic strain-dependent. Even if these signatures do not directly measure the magnetic losses, evaluating plastic strains provides experimental inputs to the numerical methods used to predict them.

The influence of plastic strain on the magnetic response of a ferromagnetic specimen has been studied in detail:

- The correlation between plasticity and dislocation density is well verified [18]. Many studies have solved the magneto/plastic strain issue by expressing each magnetic property as a dislocation density function. Scaling approaches can be used starting from the domain wall interactions and resulting in macroscopic phenomena [19][20].
- Plastic deformation is also a source of internal stress. Other methods rely on this property, and numerical tools have been developed to determine the effect of the mechanical stress [21].
- However, most researchers still favor phenomenological approaches that establish analytical expressions relating the change in magnetic parameters to the plastic strain [22]-[24].

The dislocation density increases significantly with plastic strain (Fig. 13 in [25]), but this evolution is irregular in most conventional ferromagnetic steels. However, for electrical steels, simulation and experiment have shown high precision by considering some magnetic parameters

proportional to the square root of the dislocation density. For instance, the study in [26] successfully set the Jiles–Atherton model parameter of the coercive field, k, and the hysteresis loss parameter, a, to be proportional to the square root of the dislocation density:

$$k, a \propto (\text{dislocation density})^{0.5} = \sqrt{\text{dislocation density}}\,. \quad (1)$$

In [27], the dislocation density was not reported, but tests on commercial fully-processed electrical steel specimens showed that the hysteresis loss, eddy current loss, and effective permeability depend on the square root of the rolling plastic strain:

$$W_{hy}, W_{cl}, \mu_{eff} \propto (\text{rolling plastic strain})^{0.5}\,. \quad (2)$$

These observations are essential for our study, which assumes these relations between the magnetic losses and the plastic strain in electrical steel.

In this work, we put simulations and predictions aside and focused on experimental observations. Magnetic non-destructive controls are already industrially used to detect plastic strain defects [28]-[30]. Different magnetization signatures have already been tested:

- Averaged quantities such as magnetic losses [27][31].
- Local behaviors such as magnetic Barkhausen noise (MBN) [32][33] and magnetic incremental permeability (MIP) [29][34].

However, the most valuable indicator is still difficult to identify because all these results come from distinct specimens and experimental conditions.

The magnetic response is highly sensitive to environmental conditions such as temperature and to the sample history [35]. Barkhausen noise reproducibility has, for instance, already been observed in thin ferromagnetic films where magnetic states are easier to control [36]-[38], but never in bulky samples.

This study used the same experimental conditions (sensor, magnetization yoke, and signal treatment) to limit the degrees of freedom. We measured the impact of plastic strain on three distinct magnetic signatures: the MIP, MBN, and classic $B_a(H_{surf})$ hysteresis loops, where B_a is the average cross-sectional flux density, and H_{surf} is the surface tangential excitation field. Hysteresis cycles were reconstructed for all these observations, and specific indicators such as the coercivity, hysteresis area, and remanence were plotted versus plastic strain. Correlations were established, and the most appropriate indicators were selected. Then, additional experimental tests were run to confirm the viability of the proposed indicators in NDT conditions.

This study was restricted to NO FeSi specimens to avoid additional effects due to the GO FeSi Goss texture. Even if there is still a small recurrent anisotropy, it can be neglected. The magnetic behavior can be characterized in any direction, and the impact of plastic strains is easier to observe.

The paper is organized as follows: Section 2 describes the experimental setup and briefly introduces the tested specimens. Section 3 gives the experimental results and the correlations between the magnetic and mechanical properties. The last section presents discussions and conclusions.

2 Materials and methods

2.1 Specimens

NO FeSi electrical steel laminae (35JNE250 from JFE Engineering Cooperation, Tokyo, Japan) were tested in this study. All specimens were extracted from the same batch. Table 1 gives their physical properties as provided by the manufacturer.

Table 1. Physical properties of 35JNE250 (JFE catalog).

	Thickness (mm)	Density ($kg.dm^{-3}$)	Resistivity ($\mu\Omega \cdot cm$)	Core loss at 50 Hz ($W \cdot kg^{-1}$)		Min. magnetic flux density at 5000 $A \cdot m^{-1}$ (T)	Min. Lamination Factor (%)
Grade				1 T	1.5 T		
35JNE250	0.35	7.65	47	1.02	2.3	1.67	95

Yield point ($N \cdot mm^{-2}$)		Tensile Strength ($N \cdot mm^{-2}$)		Elongation %		Hardness HV (1 kg)
L	C	L	C	L	C	
351	356	489	504	27	28	182

"L" and "C" mean the directions parallel and transverse to the rolling direction, respectively.

Initially, 10 strips were cut in Epstein frame dimensions (160 x 30 x 0.35 mm^3) by electrical discharge machining (EDM) to get bone-shaped specimens for tensile test measurements Fig. (1)]. No mechanical contact is involved in EDM cutting, resulting in an invariant internal stress and absence of induced plastic strain.

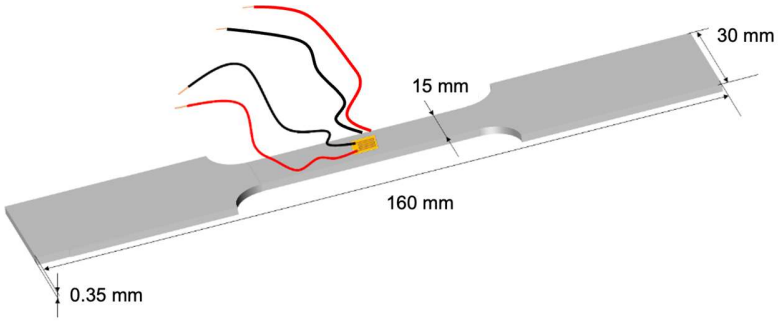

Fig. 1. 3D view and dimensions of the tensile stress specimens.

The center of each specimen was polished slightly with emery paper #240 to improve the adhesion, and two strain gauges were bonded to measure the strain.

2.2 Experimental setup

An experimental setup was built to provide multiple magnetic signatures. The same inductor, sensors, and controllers were used for all tests. The IEC 60404-3 standard uses a single sheet tester to characterize an electrical steel lamina [39]. Even if differences exist (such as in dimension or H_{surf} measurement), our setup (Fig. 2, top-right side) is inspired by this standard.

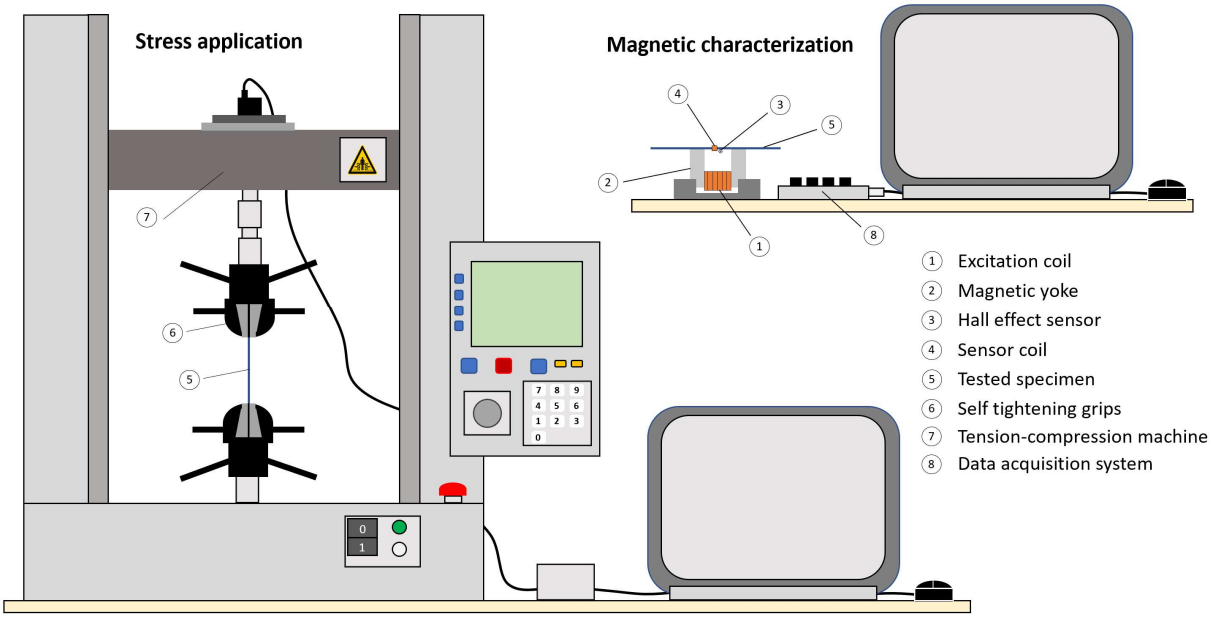

Fig. 2. Overall 2D view of the experimental setup.

2.2.1 Tensile stress

A tension–compression machine (TENSILON RTC-1250, A&D Company, Tokyo, Japan) was used to apply tensile stress (Fig. 2, left side). All tests were done at room temperature. The plastic strain was measured using the strain gauges bonded to the surface of each tested specimen (Fig. 1). A preliminary mechanical characterization was performed up to rupture (close to 9.9 % strain) to obtain a large-scale strain–stress curve. This curve is shown in Fig. 3 and served as the mechanical reference for the subsequent tests.

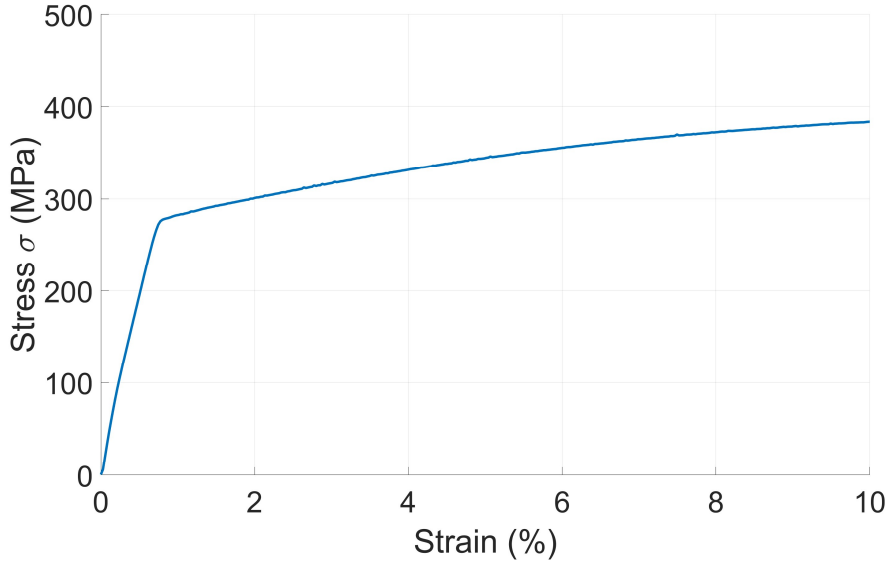

Fig. 3. Stress–strain reference curve for the NO FeSi 35JNE250 specimens.

Then, a series of tests was performed:

- Five specimens were mechanically loaded to reach five levels of plastic strain (0, 1%, 2.9%, 5.5%, and 9.4%). Once unloaded, they were removed from the tension–compression machine and magnetically tested using the characterization setup at the top-right of Fig. 2.

Every magnetic test was repeated two times to check the reproducibility.

2.2.2 Magnetic excitation

The magnetic source was the same for all experimental tests, including the last in NDT conditions. The magnetic inductor consisted of a U-shaped 3 wt.% FeSi yoke. The leg size of the yoke was 37 mm × 37 mm, and the inner distance between the legs was 69 mm. The tested specimens were set free to move. The excitation coil was wound around the yoke and supplied by a power amplifier (HSA 4014, NF Corporation, Yokohama, Japan) driven by a frequency

generator (Agilent 33220A, Santa Clara, CA, USA). The yoke and the specimen roughness were low enough to ensure good magnetic contacts and avoid reproducibility issues due to surface quality.

2.2.3 Magnetic instrumentation

a) $B_a(H_{surf})$ major hysteresis cycles

The tangential magnetic field H_{surf} was measured locally on the surface of each tested specimen in the field direction using a Hall element sensor (SS94A, Honeywell, Charlotte, NC, USA). The magnetic response of the hall element was pre-characterized using a Helmholtz coil driven by a current source in DC mode.

All the tested specimens were wound with n = 100 turns of a sensor coil. The voltage drop due to the magnetization variation was recorded using a scope (Tektronix, Beaverton, Oregon, USA). B_a was obtained by numerically integrating the equation

$$B_a(t) = -\frac{1}{n \cdot S}\int_0^t e(t)dt\,, \tag{3}$$

where S is the cross section, and e is the electromotive force. A numerical correction was done to cancel the undesired drift due to the ambient noise and the integration.

Concerning the magnetic source, the frequency generator fed the power amplifier with a 100-mHz sinusoidal voltage. The magnetic excitation waveform was not controlled. The frequency was supposed to be low enough to maintain the magnetization in a quasi-static state, and the results were independent of the excitation waveform.

b) $B_{MIP}(H_{surf})$ hysteresis cycles

The reversible permeability was obtained from the impedance of the coil surrounding the material under testing. The MIP was produced by superimposing the coil's small amplitude and high-frequency magnetic field excitation onto a high, quasi-static magnetic field produced by the magnetic yoke [40]. The mathematical expression for the MIP, μ_{MIP}, is

$$\mu_{MIP} = \frac{1}{\mu_0} \cdot \frac{\Delta B_a}{\Delta H_{surf}} \ , \tag{4}$$

where μ_0 is the vacuum permeability.

The sensor coil impedance was measured using an LCR meter (ZM2375, NF Corporation, Yokohama, Japan) for the MIP characterization. The electrical current in the sensor coil was set to I_{RMS} = 10 mA, inducing a magnetic excitation lower than a quarter of the coercivity (as recommended in the literature [41]). The frequency of the alternating contribution was set to 50 kHz. The resulting data provided by the LCR meter consisted of the sensor coil impedance modulus, phase, and real and imaginary parts. The MIP was obtained from the equations

$$Z_{MIP} = Z'_{MIP} + jZ''_{MIP} = R + jL\omega \ , \tag{5}$$

$$L = \frac{n^2 \cdot \mu_{MIP} \cdot S}{l} , \tag{6}$$

and B_{MIP} was obtained by integrating

$$B_{MIP}(t) = \int_{H_{surf}=0}^{H_{surf}=t} \mu_{MIP}(t) dH_{surf} \ , \tag{7}$$

where R and L are the sensor coil resistance and inductance, respectively; ω is the angular frequency; and l is the inner distance separating the yoke legs. Eddy currents are neglected in Eq. 6. The maximum value of μ_{MIP_r} was approximately 75, which at 50 kHz leads to a skin depth 180 µm greater than half the tested specimen's thickness.

Calibration was carried out to consider the parasitic impedances due to the electrical wires and contacts. The MIP μ_{MIP} and differential permeability μ_{DIF} are identical in the saturated regime; thus, μ_{MIP} was corrected with an additional constant factor to ensure this condition.

The quasi-static excitation waveform was not controlled. The frequency was 100 mHz, and the magnetization process was supposedly frequency-independent.

c) $MBN_{energy}(H_{surf})$ hysteresis cycles

During the magnetization process, the domain wall motions are stochastic. The MBN raw signal is unpredictable and not reproducible. This problem is solved using time-averaged indicators such as the root mean square (RMS) and raw signal envelope for the MBN analysis. In this study, we opted for the Magnetic Barkhausen Noise energy, MBN_{energy} [42][43]:

$$MBN_{energy}(t) = \int_0^t sign\left[\frac{dH_{surf}}{dt}(s)\right] V_{MBN}^2(s)\, ds\,, \tag{8}$$

where V_{MBN} is the electromotive force of the sensor coil after filtering and amplification. The process for constructing the MBN_{energy} hysteresis loop from the raw MBN measurement is illustrated in Fig. 4.

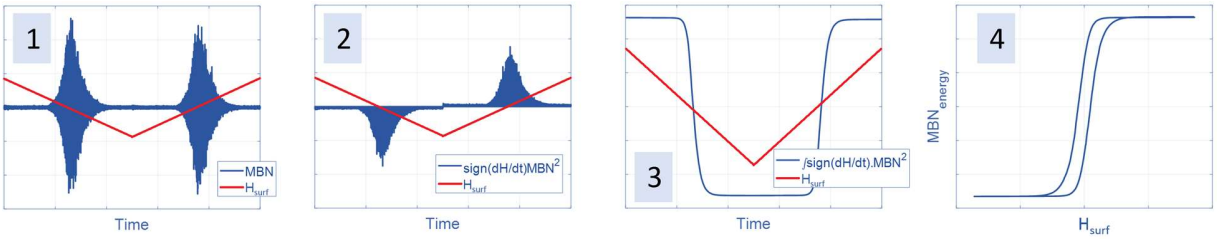

Fig. 4. $MBN_{energy}(H_{surf})$ hysteresis loop and construction process.

MBN_{energy} is not an energy *per se*, but as explained in [41], it can be used to represent the kinetic energy of the domain walls. It is possible to renormalize the MBN_{energy} measurement to

compare $MBN_{energy}(H_{surf})$ and the standard $B_a(H_{surf})$ hysteresis loops. There are two options for this renormalization:

- Equalizing the hysteresis areas, assuming the domain wall motions are fully responsible for the hysteresis loss contribution.
- Equalizing the beginning of the saturation elbow (where the rotation is supposed to start) and considering rotation as a source of hysteresis loss.

During the experiment, MBN_{energy} was determined by combining analogical and numerical procedures:

- The raw electromotive force of the sensor coil was filtered and amplified using a Stanford Research SR650 filter (Sunnyvale, CA, USA). The cut-off frequencies were set to 500 and 5 kHz, and the gain to 40 dB·dec^{-1}.
- The squaring (Step 2 in Fig. 4), integration (Step 3 in Fig. 4), and drift correction were done numerically using Matlab®.

All the data were averaged over four excitation periods to reduce the parasitic noises. The magnetic excitation was the same as in subsections 2.2.3a and b.

3 Correlation results

3.1 $B_a(H_{surf})$ hysteresis cycles

The first magnetic experimental results presented in this paper are the $B_a(H_{surf})$ hysteresis cycles (Fig. 5a–d) and the related losses (hysteresis areas in Fig. 5e and f) for the five tested specimens. Max(B_a) (maximum cross-sectional flux density) was sequentially set to 0.7 T, 1.0 T, 1.3 T, and 1.5 T. We opted for f = 100 mHz, close to the quasi-static threshold, to avoid undesired

dynamical effects [44] and limit the magnetic loss to the quasi-static contribution [45]. For comparison, the same excitation waveform was imposed for the MIP and MBN characterizations.

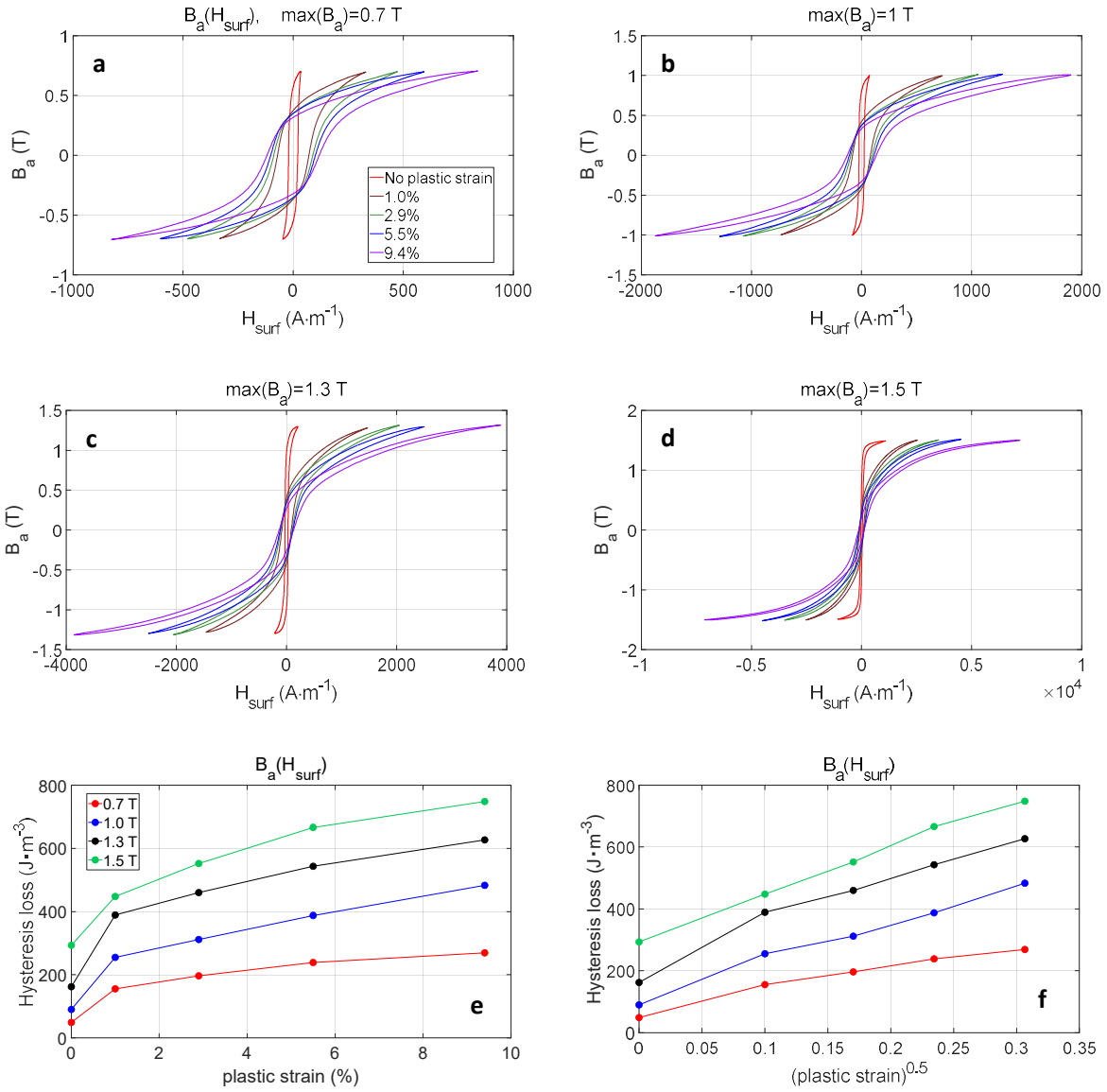

Fig. 5. (a), b), (c), and (d) Quasi-static hysteresis cycles for the five tested specimens with max(B_a) = 0.7, 1, 1.3, and 1.5 T, respectively. (e) Hysteresis loss as a function of plastic strain. (f) Hysteresis loss as a function of (plastic strain)$^{0.5}$.

The rise in the plastic strain leads to an increase in the hysteresis loss contribution. A quasi-linear fit is obtained by plotting this contribution as a function of (plastic strain)$^{0.5}$ (Fig. 5f). This has already been observed in other studies [25][28].

3.2 $B_{MIP}(H_{surf})$ hysteresis cycles

Fig. 6 shows the MIP characterization for the five specimens obtained with the experimental setup and the numerical treatment described in subsection 2.2.3. Hysteresis cycles are shown in the top plots (Fig. 6 a–d) and the corresponding losses in the bottom ones (Fig. 6e and f).

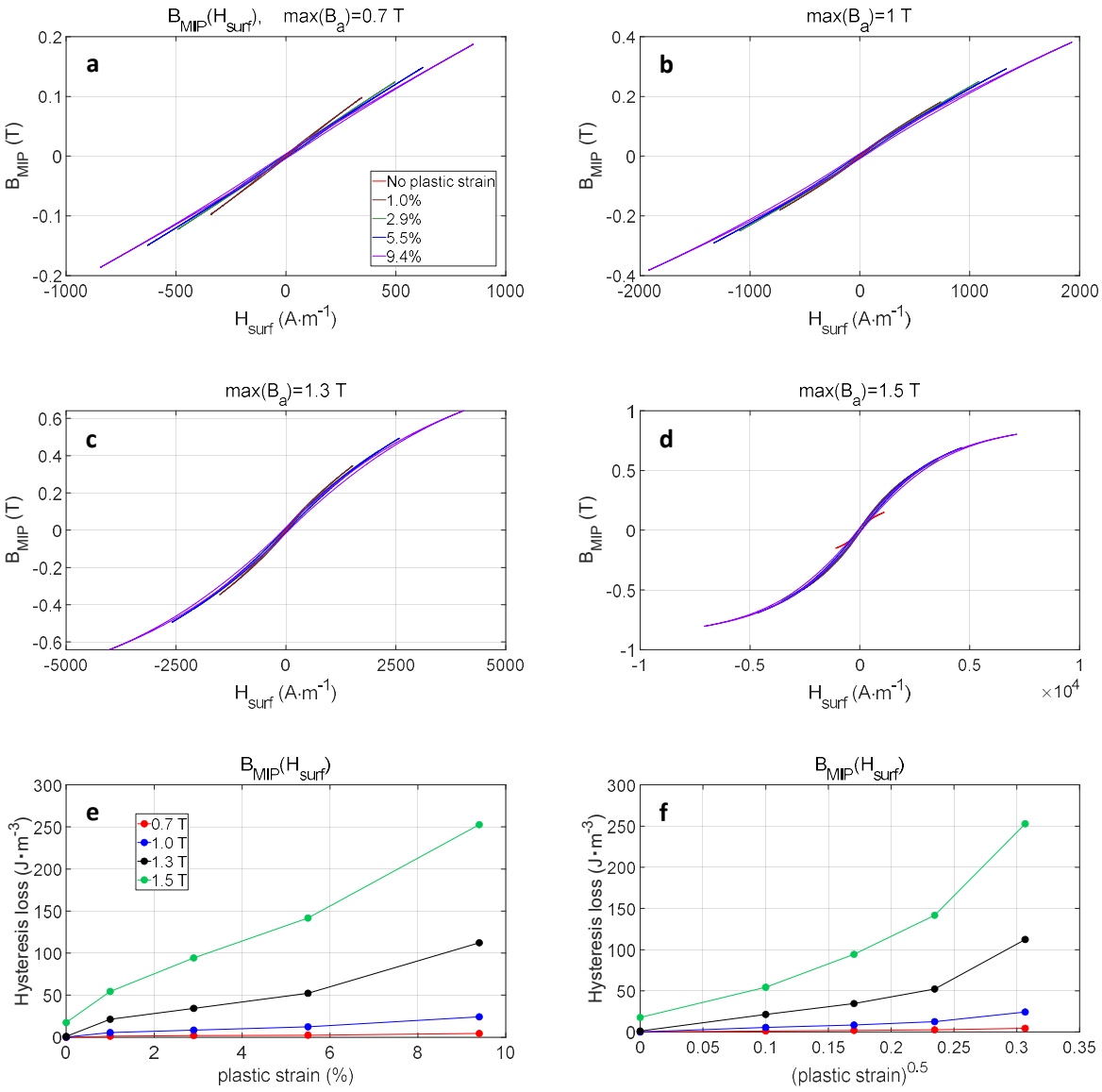

Fig. 6. (a), (b), (c), and (d) MIP hysteresis cycles for the five tested specimens with max(B_a) = 0.7, 1, 1.3, and 1.5 T, respectively.
(e) MIP hysteresis loss as a function of plastic strain. (f) MIP hysteresis loss as a function of (plastic strain)$^{0.5}$.

3.3 $MBN_{energy}(H_{surf})$ hysteresis cycles

Fig. 7 depicts the $MBN_{energy}(H_{surf})$ hysteresis cycles for the five specimens obtained with the experimental setup and the numerical treatment described in subsection 2.2.3. MBN_{energy} has intentionally not been renormalized to keep the possibility of using the hysteresis area and remanence as plastic strain indicators. Hysteresis cycles are shown in the top plots (Fig. 7a–d) and the corresponding losses in the bottom ones (Fig. 7e and f).

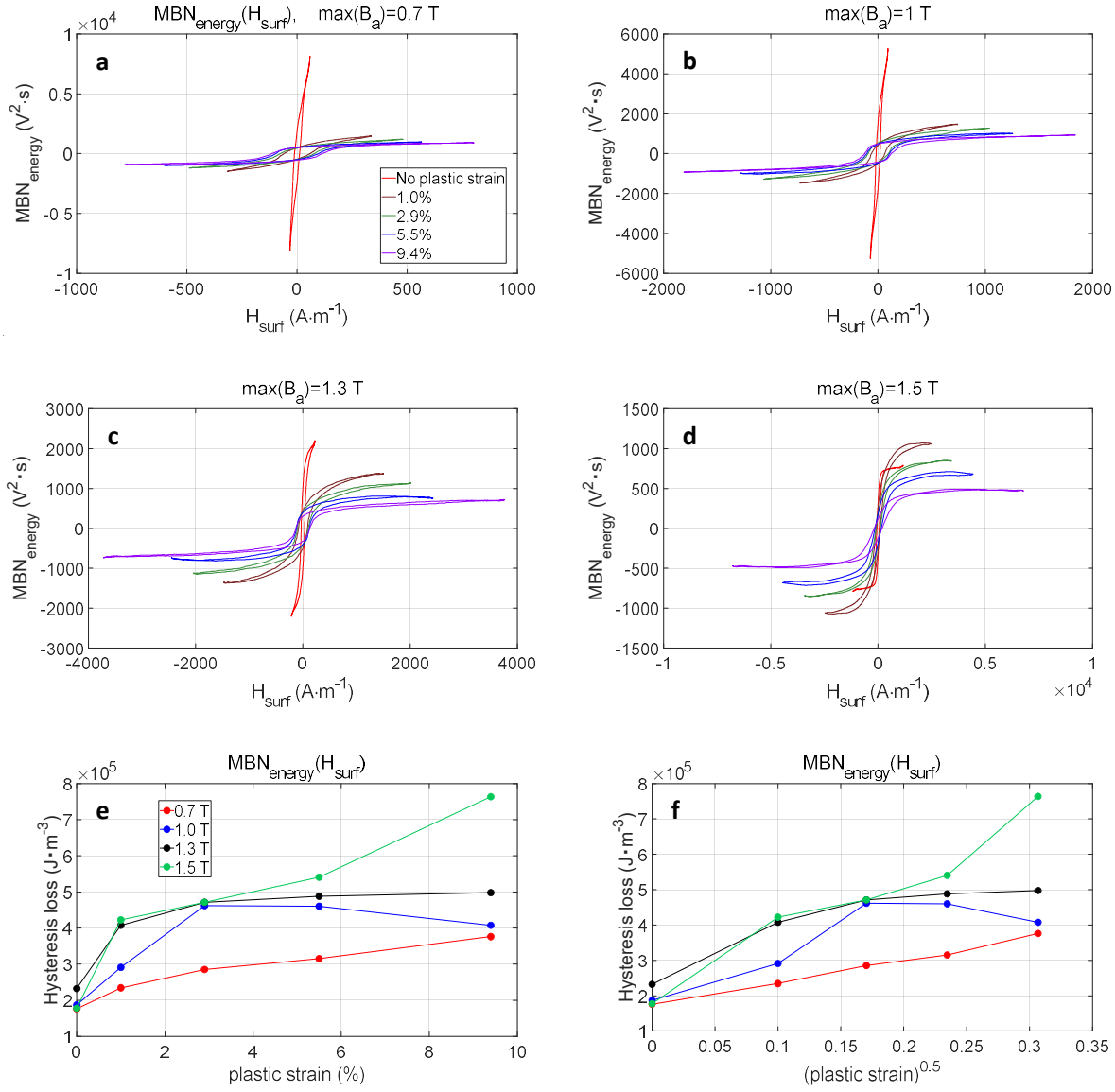

Fig. 7. (a), (b), (c), and (d) MBN_{energy} hysteresis cycles for the five tested specimens with max(B_a) = 0.7, 1, 1.3 and 1.5 T, respectively. (e) MBN_{energy} hysteresis loss as a function of plastic strain. (f) MBN_{energy} hysteresis loss as a function of (plastic strain)$^{0.5}$.

3.4 Magnetic indicators as functions of the plastic strain

International standards govern $B_a(H_{surf})$ hysteresis cycle characterization. These recommendations include working under an imposed sinusoidal B_a [39][46][47]. The $B_a(H_{surf})$ hysteresis cycle represents the magnetization mechanism by itself, but it also opens access to specific indicators such as the coercivity and remanence. By obtaining hysteresis cycles in the same experimental conditions as those of the MBN and MIP measurements, additional indicators can be accessed, and correlations can be established with the targeted property: plastic strain. Fig. 8 introduces the indicators we opted for, and Fig. 9 shows the evolution of these indicators as functions of plastic strain and of (plastic strain)$^{0.5}$ for the three magnetic signatures tested. Pearson correlation coefficients are calculated and shown in Fig. 10 to verify the linear relationship between these indicators and plastic strain or (plastic strain)$^{0.5}$.

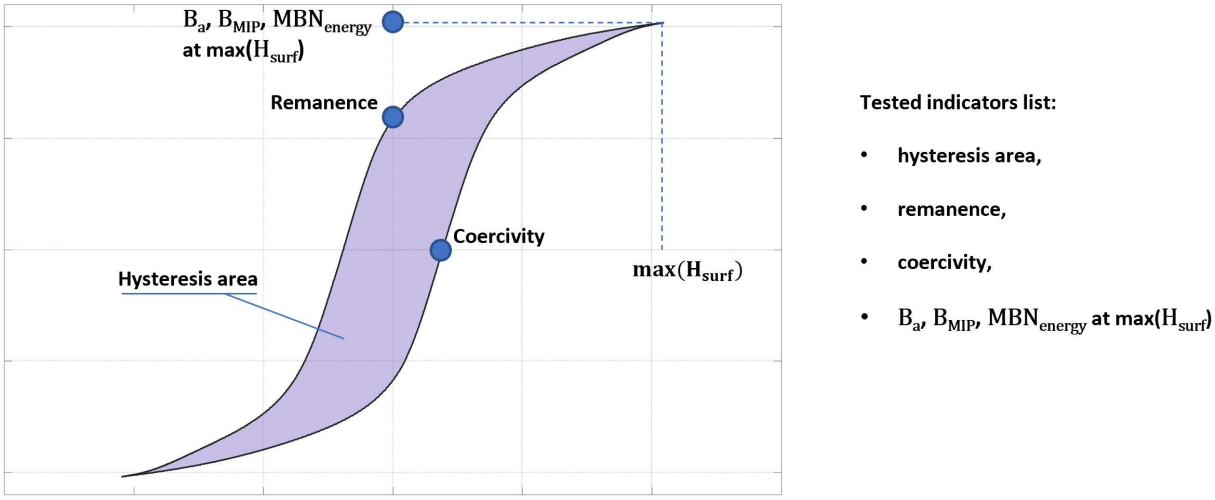

Fig. 8. List and illustration of the tested magnetic indicators.

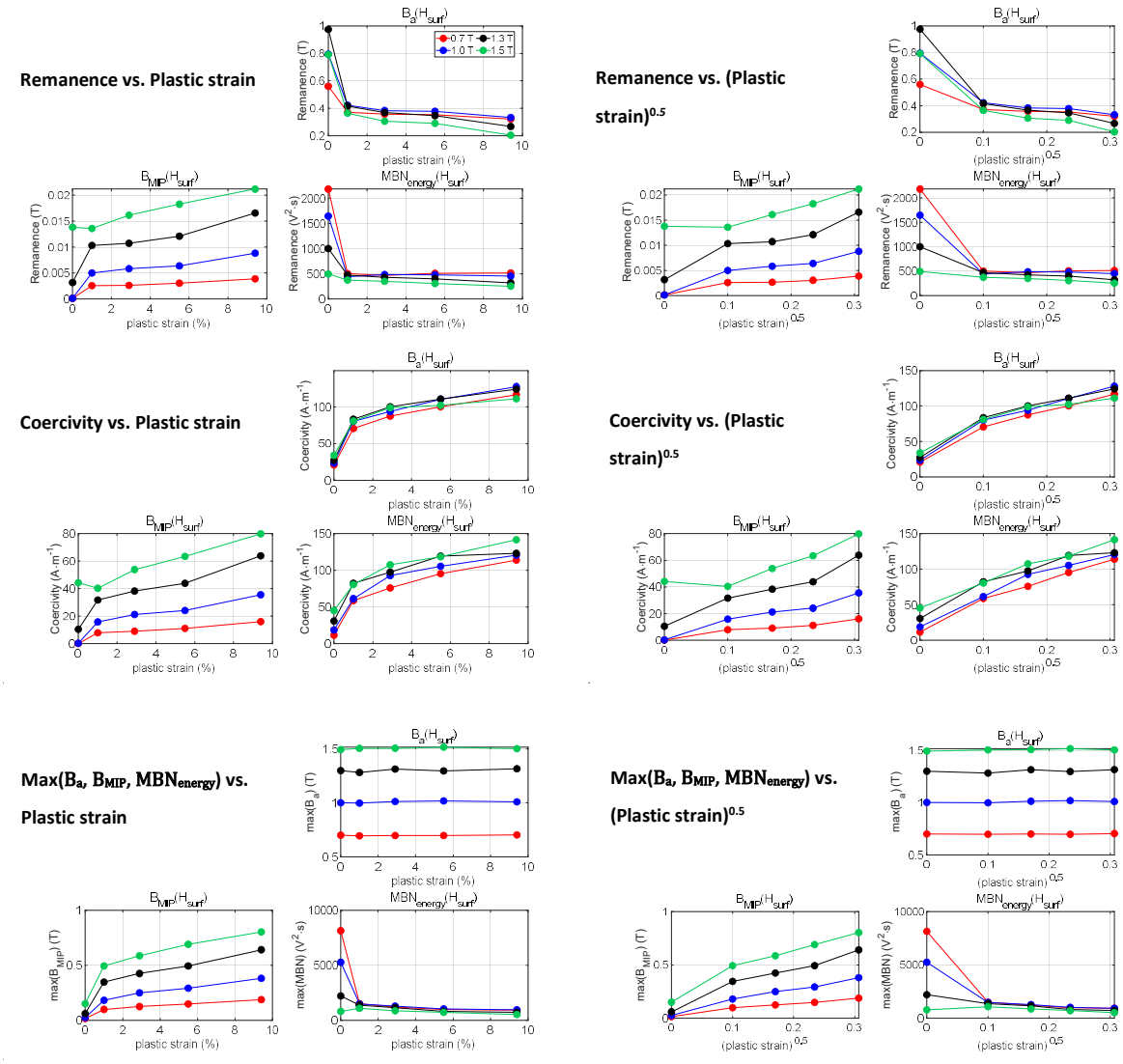

Fig. 9. Left: Tested coefficients vs. plastic strain. Right: Tested coefficients vs. (plastic strain)$^{0.5}$.

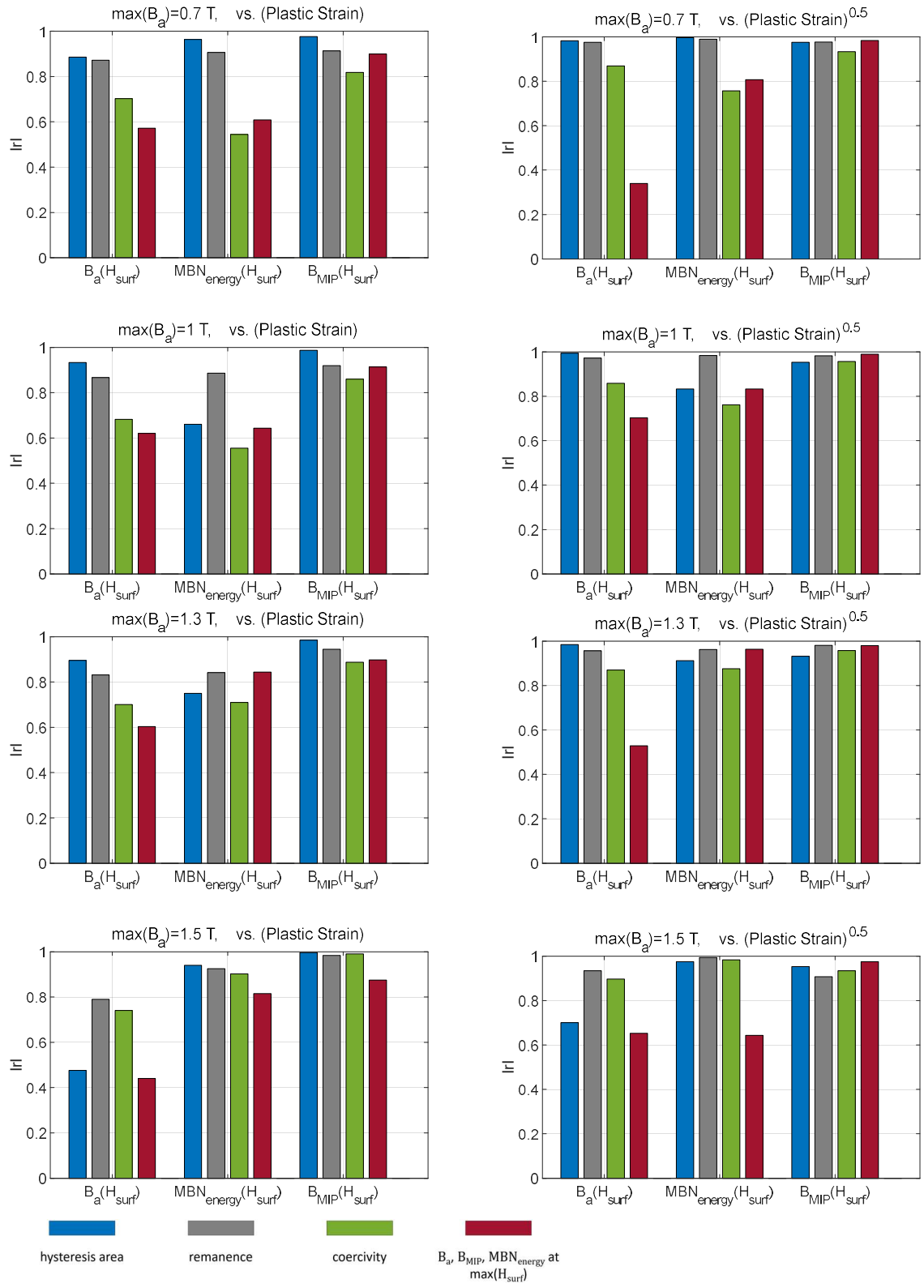

Fig. 10. Pearson correlation coefficients (|r|) for all the magnetic indicators vs. plastic strain (left) and vs. (plastic strain)$^{0.5}$ (right).

4 Discussion and conclusions

4.1 Plastic strain vs. magnetization mechanisms

A ferromagnetic material's magnetization process supports multiple mechanisms. First, the magnetic domains with a magnetization oriented favorably to the applied magnetic field grow, while the domains unfavorably oriented decline in proportion. Then, the magnetization of the resulting domain, initially oriented along an easy axis, coherently rotates toward the direction of the applied magnetic field. The vast majority of the magnetization mechanisms are associated with the magnetic domains and their distribution, including:

- **Domain wall bulging** (**DWB**, low H_{surf} amplitude range)[48][49],
- **Domain wall irreversible motions** (**DWIM**, middle H_{surf} amplitude range)[50],
- **Domain nucleation** and **fusion** (**DNF**, high H_{surf} amplitude range),
- **Domain wall dynamic response** (**DWDA**), frequency dependence, ripples, and avalanches (AC H_{surf})[51]-[54].

The other mechanisms are independent of the magnetic domain structure:

- **Magnetization rotation** (**MR**, high H_{surf} amplitude range)[50].
- **Macroscopic eddy currents** (**MEC**, AC H_{surf})[55].

The magnetic indicators described in subsection 3.4 do not equally depend on the magnetization mechanisms. Table 2 links these indicators to their main contributors. The absence of **DNF**, **DWD**, and **MEC** is worth noting. **DNF** cannot be feasibly observed with macroscale magnetic characterization equipment, and the energy exchanges related to this mechanism are weak.

In the low-frequency range below the quasi-static threshold, the losses associated with the hysteresis area are only due to **DWIM**. **MR** is independent of magnetic domain kinetics, and the energy transfers related to this mechanism are assumed to be negligible.

Magnetic domains change their size when the domain walls move within the crystal lattice in response to a variation in magnetic excitation. Local defects form temporary barriers causing the domain wall to be hung up. When the magnetic field becomes strong enough, it causes a group of atoms to flip their spin at once as the domain wall "snaps" past the defect. When monitored with a sensor coil, the accumulation of these local irreversible changes in magnetization (**DWIM**) gives rise to the MBN raw signal. Thus, MBN and **DWIM** are strongly linked, and in this study, we supposed that all $MBN_{energy}(H_{surf})$ indicators were linked to this magnetization mechanism.

The experimental setup description states that the MIP sensor coil is supplied by a weak electrical current I_{RMS} = 10 mA. However, it is supposed to be strong enough to induce **DWB** but not **DWIM**. Most $B_{MIP}(H_{surf})$ indicators can thus be associated with **DWB**.

Coercivity is a consequence of the magnetic losses; therefore, it is always due to **DWIM** in the low-frequency range. This observation is valid regardless of the magnetic signature tested.

Finally, the remanence read on $B_a(H_{surf})$ is linked to the magnetic losses and **DWIM**. It is also due to **MR,** whose contribution is significant in the anhysteretic behavior beyond the saturation elbow.

Table 2. Magnetic indicators and their main contributing magnetization mechanisms.

	$B_a(H_{surf})$	$B_{MIP}(H_{surf})$	$MBN_{energy}(H_{surf})$
Hysteresis area	DWIM	DWB	DWIM
Remanence	DWIM/MR	DWB	DWIM
Coercivity	DWIM	DWIM	DWIM
B_a / B_{MIP} / MBN_{energy} at max. (H_{surf})	DWIM/MR	DWB	DWIM

All the magnetization mechanisms are sensitive to plastic strain, but their sensitivity levels differ. Plastic strain identification can be improved by isolating the mechanism of higher sensitivity. For this, the first step defines experimental situations and indicators where each magnetization mechanism is dominant (Table 2).

Most researchers have limited their tests to the standard characteristic signatures: $B_a(H_{surf})$ hysteresis cycles and the associated magnetic losses [38][46][47]. Unfortunately, the mechanisms superimpose and interact during a magnetization cycle, making unique observation of $B_a(H_{surf})$ impossible to use to identify the mechanism. However, specific indicators like coercivity or magnetic losses can provide specific information. The magnetic losses can, as an example, be separated according to the statistical theory of losses (STL), and each contribution can be correlated with plastic strain:

- W_{cl}, the classic loss term, is associated with **MCE**.
- W_{ex}, the excess loss term, is associated with **DWDA**.
- W_{hy}, the hysteresis loss term, is frequency-independent and associated with **DWIM**.

No tests have been run to check the plastic strain influence on W_{cl} and W_{ex}. However, convergent results from the literature show low sensitivity for both of these contributions (Fig. 6

in [45] for W_{cl}, [28] and Fig. 11 in [45] for W_{ex}). This observation confirms that **MCE** and **DWD** can be removed from the list of ideal magnetization mechanisms.

By contrast, our study has demonstrated and verified a strong correlation between W_{hy} and the square root of the plastic strain (Fig. 5f). W_{hy} is due to domain wall motions in the low-frequency range. Reversible (DWB) but mostly irreversible (**DWIM**) motions contribute to W_{hy}.

W_{hy} is a powerful indicator but difficult to use in an NDT context where experimental conditions forbid standard $B_a(H_{surf})$ characterization. However, these first conclusions can lead us toward an ideal indicator.

In the next step, the Pearson correlation coefficients in Fig. 10 are condensed into a single figure (Fig. 11) and averaged between the different magnetization levels.

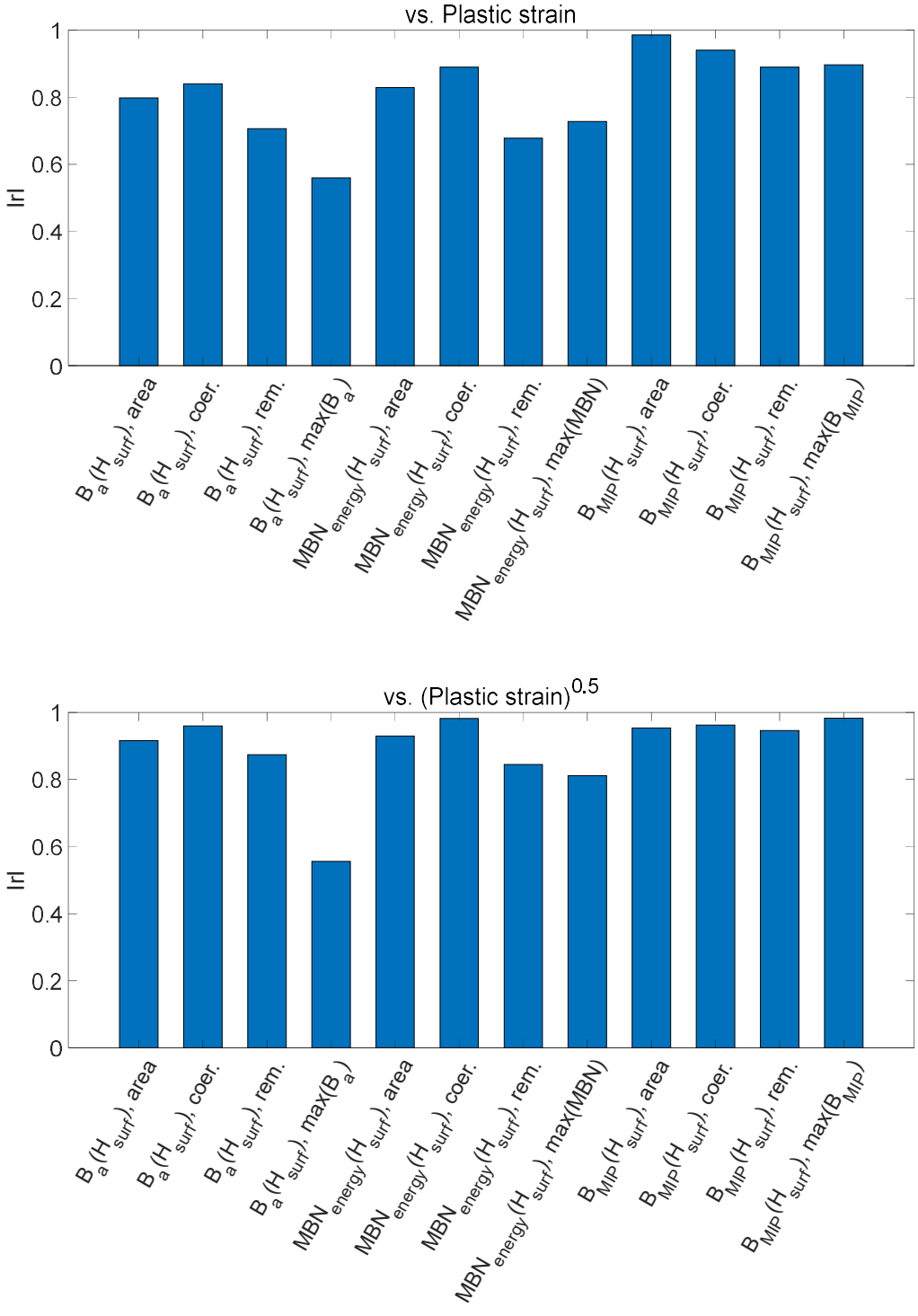

Fig. 11. Averaged Pearson coefficients for all the magnetic indicators.

The plastic strain's most sensitive indicator was the hysteresis loop area of $B_{MIP}(H_{surf})$ (IrI = 0.9825). The most sensitive indicators of (plastic strain)$^{0.5}$ were max(B_{MIP}) and $MBN_{energy}(H_{surf})$ coercivity, with IrI = 0.9825 and IrI = 0.9822, respectively. Among these three indicators, those of MIP are linked to **DWB** and those of MBN to **DWIM**. A high correlation was not really expected for Max(B_{MIP}). By contrast, the indicator of $MBN_{energy}(H_{surf})$ coercivity associated with **DWIM** could be predicted.

4.2 Validation of the selected indicators in an NDT context using a surface sensor

Surface tests with pancake coils (Fig. 14) were run to confirm the sensitivity of the supposedly best indicators in an NDT situation. The pancake coil was used to generate the high-frequency contribution to the MIP measurements. This coil had an inner diameter of 3.3 mm, an outer diameter of 3.95 mm, a height of 3.0 mm, a wire thickness of 0.05 mm, and 275 turns. The lift-off was 0.39 mm.

$B_{MIP}(H_{surf})$ hysteresis cycles were plotted using the process described in section 2.2.3 (with the same magnetic excitation waveform, yoke, and magnetization coils). Two indicators were tested: hysteresis area (hysteresis loss) and max(B_{MIP}). The results are plotted in Fig. 12 and the Pearson correlation coefficients in Fig. 13. Finally, the average Pearson coefficients for all magnetization levels tested were 0.9568 for the hysteresis area and 0.9294 for max(B_{MIP}).

The minor differences between the wound and the pancake coil results can be attributed to some lift-off effect. However, we can undoubtedly validate the selected indicators with Pearson coefficients higher than 0.92.

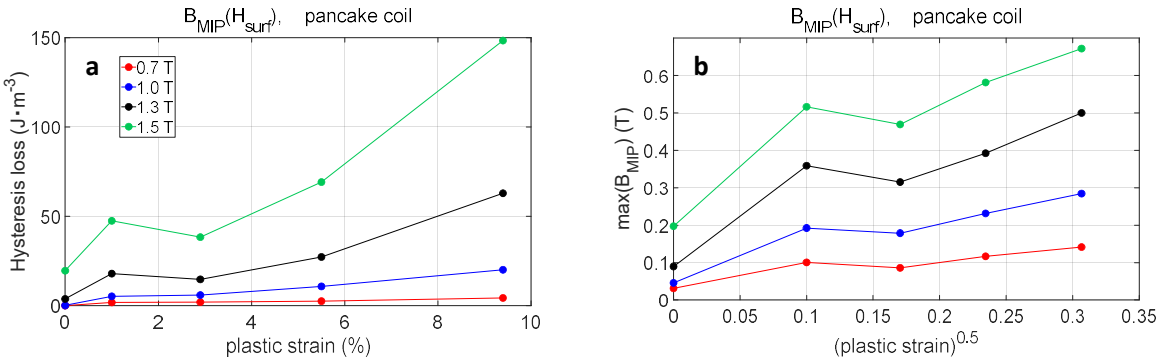

Fig. 12. Hysteresis loss as a function of the plastic strain. Fig. 12. max(B_{MIP}) as a function of the square root of plastic strain.

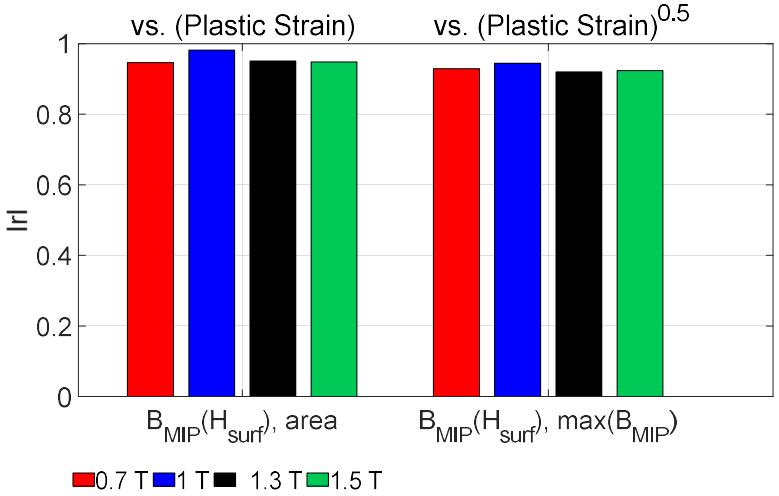

Fig. 13. Pearson correlation coefficients for the $B_{MIP}(H_{surf})$ hysteresis loss vs. plastic strain and vs. (plastic strain)$^{0.5}$, measured with the pancake coil.

For MBN measurements, a surface MBN sensor coil was used to acquire the MBN signals (Fig. 14).

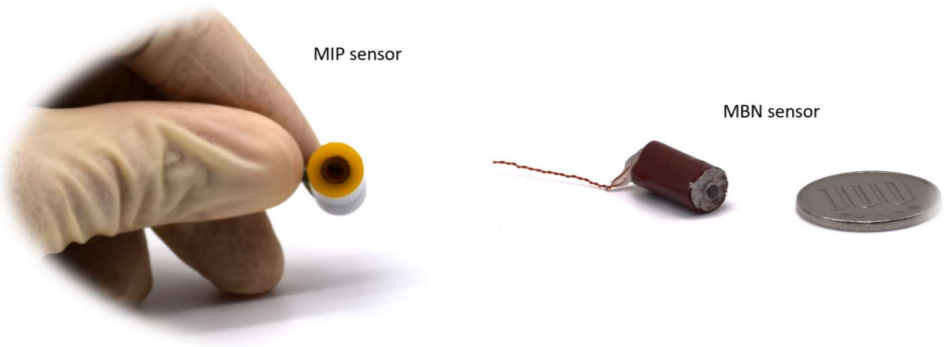

Fig. 14. Pancake coil sensor for the MIP characterization (left), and MBN sensor (right).

The test was limited to max(B_a) = 1.5 T, which gives the strongest MBN signal. We used the procedure described in section 3.3 and plotted $MBN_{energy}(H_{surf})$ hysteresis curves. Finally, a quasi-linear relationship between coercivity and (plastic strain)$^{0.5}$ was obtained (Fig. 15). The associated Pearson correlation coefficient reached the outstanding value of 0.9782.

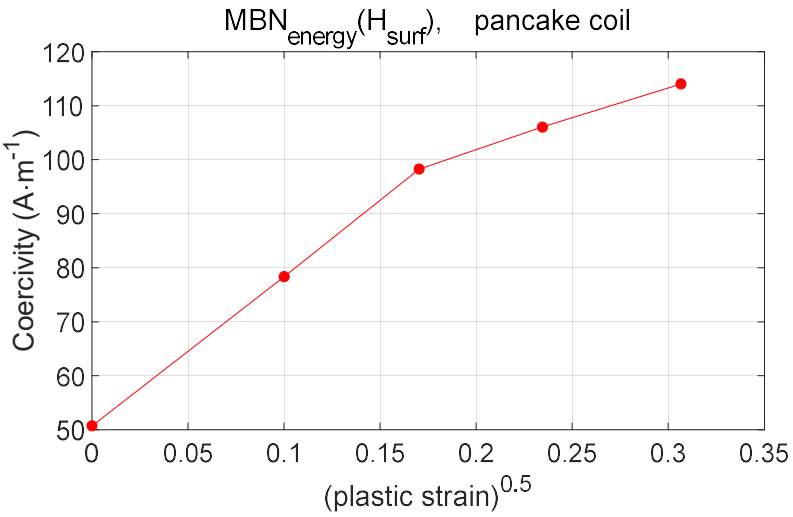

Fig. 15. Coercivity vs. (plastic strain)$^{0.5}$ for $MBN_{energy}(H_{surf})$ hysteresis curves at max(B_a) = 1.5 T.

Among the selected indicators, coercivity from $MBN_{energy}(H_{surf})$ appeared to be the most correlated indicator to plastic strain. The two indicators associated with MIP remain interesting and show an excellent linear relationship but need accurate control of the sensor lift-off.

With loss prediction being the ultimate objective, three final plots (Fig. 16) were produced to check the evolution of the selected indicators as functions of the quasi-static hysteresis loss W_{hy} [subsection 3.1, $B_a(H_{surf})$ hysteresis area]. All the resulting Pearson coefficients associated with these curves (Fig. 16, bottom right) were higher than 0.975, confirming our expectations and these indicators' ability to predict hysteresis loss measured in NDT conditions.

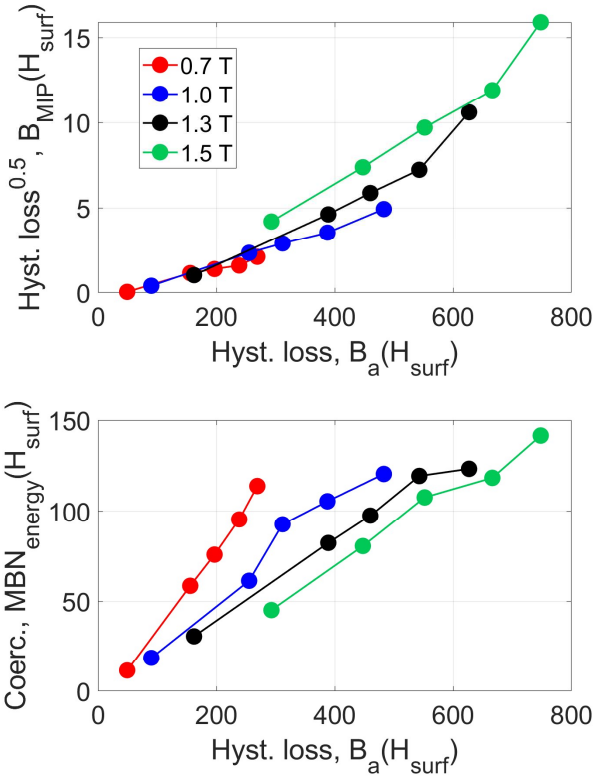

Irl: vs. Hyst. loss, $B_a(H_{surf})$

	Hyst. loss$^{0.5}$ $B_{MIP}(H_{surf})$	max(B_{MIP})	coerc. $MBN_{energy}(H_{surf})$
0.7 T	0.9895	0.9958	0.9986
1.0 T	0.9972	0.9959	0.9829
1.3 T	0.9781	0.9989	0.9904
1.5 T	0.9851	0.9829	0.9918
AV. ± STDEV	0.9874 ± 0.0069	0.9934 ± 0.0062	0.9909 ± 0.0056

Fig. 16. Selected indicators vs. $B_a(H_{surf})$ hysteresis loss and the associated Pearson correlation coefficients.

4.3 Conclusion

This study tried to develop an efficient way to detect plastic strain and magnetic loss from magnetization measurements in NDT conditions. Classic approaches focus on a unique magnetic signature and establish the relationship between the magnetic observations and the targeted property. Changes in the experimental conditions are inevitable in NDT conditions, and it is impossible to identify precisely the best magnetic indicator. In this work, we opted for a different strategy. The magnetization mechanisms were listed. Specific experimental situations using similar devices and instruments were tested to isolate those mechanisms. All magnetic indicators were plotted as functions of plastic strain and (plastic strain)$^{0.5}$. The (plastic strain)$^{0.5}$ dependence of the quasi-static losses contribution [28][45] was confirmed. This result is interesting from a theoretical viewpoint. It is, however, difficult to implement in an industrial environment because it requires wound coils and feedback control of the induction field. Other indicators showed excellent correlation, especially those linked to the magnetization mechanism associated with DWB (area and max(B_{MIP}) for MIP characterization), and DWIM (coercivity for MBN measurement). The domain walls directly interact with the dislocations, and such correlation can be predicted.

For comparison, this study used first the same wound coil but MBN and MIP characterizations need pancake coils in an NDT context. Therefore, the conclusions established with the first coil were confirmed from additional tests with a surface sensor.

Finally, we verified that ideal plastic strain indicators were also suitable for predicting hysteresis loss.

To provide further perspective for this work, it would be interesting to compare the results for magnetic loss prediction with thermal measurements, which are the only reasonable way to observe the magnetic loss aside from very recent attempts at local magnetic characterization [56].

References:

[1] K. Matsumura, B. Fukuda, “Recent developments of non-oriented electrical steel sheets,” *IEEE Trans. Magn.,* vol. 20, n° 5, pp. 1533 – 1538, 1984.

[2] J. Gyselinck, L. Vandevelde, J. Melkebeek, P. Dular, F. Henrotte, W. Legros, “Calculation of eddy currents and associated losses in electrical steel laminations,” *IEEE Trans. Magn.,* vol. 35, n° 3, pp. 1191 – 1194, 1999.

[3] G. Bertotti, “Hysteresis in magnetism,” Academic Press, Boston, 1998.

[4] N.P. Goss, US Patent, N° 1,965,559, 1934.

[5] R.M. Bozorth, “Magnetism,” Enc. Brit., vol. 14, pp. 636 – 667, 1957.

[6] X. Xiong, S. Hu, K. Hu, S. Zeng, “Texture and magnetic property evolution of non-oriented Fe-Si steel due to mechanical cutting,” *J. Magn. Magn. Mater.,* vol. 401, pp. 982 – 990, 2016.

[7] N. M’zali, T. Henneron, A. Benabou, F. Martin, A. Belahcan, “Finite element analysis of the magneto-mechanical coupling due to punching process in electrical steel sheet,” *IEEE Trans. Magn.,* vol. 57, n° 6, pp. 1 – 4, 2021.

[8] I. Gilch, T. Neuwirth, B. Schauerte, N. Leuning, S. Sebold, K. Hameyer, M. Schultz, W. Volk, “Impact of residual stress evoked by pyramidal embossing on the magnetic properties of non-oriented electrical steel,” Arch. Appl. Mech., vol. 91, pp. 3513 – 3526, 2021.

[9] H. Helbling, A. Benabou, A. Van Gorp, A. Tounzi, M. El Youssef, W. Boughanmi, D. Laloy, “Effect of industrial impregnation process on the magnetic properties of electrical steels,” *J. Magn. Magn. Mater.,* vol. 531, 16792, 2021.

[10] A. Schoppa, J. Schneider, J.-O. Roth, “Influence of the cutting process on the magnetic properties of non-oriented electrical steels,” *J. Magn. Magn. Mater.,* vol. 215 – 216, pp. 100 – 102, 2000.

[11] A. Belhadj, P. Baudouin, F. Breaban, A. Deffontaine, M. Dewulf, Y. Houbaert, “Effect of laser cutting on microstructure and on magnetic properties of grain non-oriented electrical steels,” *J. Magn. Magn. Mater.,* vol. 256, Iss. 1 – 3, pp. 20 – 31, 2003.

[12] A. Schoppa, H. Louis, F. Pude, Ch. Von Rad, “Influence of abrasive waterjet cutting on the magnetic properties of non-oriented electrical steels,” *J. Magn. Magn. Mater.,* vol. 254 – 255, pp. 370 – 372, 2003.

[13] J. Bouquerel, C. Schayes, J.B. Vogt, “Experimental mesoscopic investigation of the local cyclic plasticity of a non-oriented electrical steel,” *Mat. Sci. and Eng.: A*, vol. 820, 2021.

[14] X. Zhaosuo, Y. Kang, Q. Wang, “Developments in the production of grain-oriented electrical steel,” *J. Magn. Magn. Mater.,* vol. 320 – 323, pp. 3229 – 3233, 2008.

[15] A.J. Beaudoin, P.A. Shade, J.C. Schuren, T.J. Turner, C. Woodward, J.V. Bernier, S.F. Li, D.M. Dimiduk, P. Kenesei, J.S. Park, “Bright x-rays, reveal shifting deformation states and effects of the microstructure on the plastic deformation of crystalline materials,” *Phys. Rev. B* 96, 174116, 2017.

[16] A. S. Maderuelo, L. Castro, G. de Diego, “Plastic strain characterization in austenic stainless steels and nickel alloys by electron backscatter diffraction,” *J. Nucl. Mat.*, vol. 416, iss. 1 – 2, pp. 75 – 79, 2011.

[17] A. Moreau, D. Lévesque, M. Lord, M. Dubois, J.-P. Monchalin, C. Padioleau, J.F. Bussière, “On-line measurement of texture, thickness and plastic strain ratio using laser-ultrasound resonance spectroscopy,” *Ultrasonics*, vol. 40, iss. 10, pp. 1047 – 1056, 2002.

[18] L. Piotrowski, B. Augustyniak, M. Chmielewski, F.J.G. Landgraf, M.J. Sablik, “Impact of plastic deformation on magnetoacoustic properties of Fe–2% Si alloy,” *NDT&E Int.*, *42*(2), pp.92 – 96, 2009.

[19] A.H. Qureshi, L.N. Chaudhary, “Influence of plastic deformation on coercive field and initial susceptibility of Fe-3.25% Si alloys,” *J. of App. Phys.,* vol. 41, 1042, 1970.

[20] J.M. Makar, B.K. Tanner, “The effect of plastic deformation and residual stress on the permeability and magnetostriction of steels,” *J. Magn. Magn. Mater.,* vol. 222, iss. 3, pp. 291 – 304, 2000.

[21] O. Hubert, M. Clavel, I. Guillot, E. Hug, “Magnetism and internal stresses: concept of magneto-plastic anisotropy,” *J. Phys. IV France,* vol. 09, 1999.

[22] M.J. Sablik, S. Rios, F.J.G. Landgraf, T. Yonamine, M.F. de Campos, “Modeling of sharp change in magnetic hysteresis behavior of electrical steel of small plastic deformation,” *J. of App. Phys.,* vol. 97, 10E518, 2005.

[23] F.J.G. Landgraf, M. Emura, “Losses and permeability improvement by stress relieving fully processed electrical steels with previous small deformations,” *J. Magn. Magn. Mater.,* vol. 242 - 245, part. 1, pp. 152 – 156, 2002.

[24] J.M. Makar, B.K. Tanner, “The in situ measurement of the effect of plastic deformation on the magnetic properties of steel: Part II – Permeability curves,” *J. Magn. Magn. Mater.,* vol. 187, Iss. 3, pp. 353 – 365, 1998.

[25] A. Daem, P. Sergeant, L. Dupré, S. Chaudhuri, V. Bliznuk, L. Kestens, “Magnetic properties of silicon steel after plastic deformation,” *Materials,* vol. 13, 4361, 2020.

[26] L. Dupré, M. Sablik, R. Van Keer, J. Melkebeek, “Modeling of microstructural effects on magnetic hysteresis properties,” *J. Phys. D Appl. Phys.,* vol. 35, n° 17, pp. 2086, 2002.

[27] C.K. Hou, S. Lee, “Effect of rolling strain on the loss separation and permeability of lamination steels,” *IEEE Trans. Magn.,* vol. 30, n° 1, pp. 212 – 216, 1994.

[28] G. Dobmann, “Physical basics and industrial applications of 3MA-micromagnetic multiparameter microstructure and stress analysis,” Proc. ENDE Conf., pp. 1 – 12, 2007.

[29] T. Matsumoto, T. Uchimoto, T. Takagi, G. Dobmann, B. Ducharne, S. Oozono, H. Yuka, “Investigation of electromagnetic non-destructive evaluation of residual strain in low carbon steels using the eddy current magnetic signature (EC-MS) method,” *J. Magn. Magn. Mater.,* vol. 479, pp. 212 – 221, 2019.

[30] S. Takeda, T. Uchimoto, A. Kita, T. Matsumoto, T. Sasaki, Mechanism study of the residual stress evaluation of low-carbon steels using the eddy current magnetic signature, *J. Magn. Magn. Mater.,* vol. 538, 168268, 2021.

[31] D.L. Rodrigues-Jr, J.R.F. Silveira, G.J.L. Gerhardt, F.P. Missel, F.J.G. Ladgraf, R. Machado, M.F. de Campos, “Effect of plastic deformation on the excess loss on electrical steel,” *IEEE Trans. Magn.,* vol. 48, n° 4, pp. 1425 – 1428, 2012.

[32] O. Stupakov, T. Takagi, T. Uchimoto, “Alternative magnetic parameters for characterization of plastic tension,” *NDT&E Int., 43*(8), pp.671-676, 2010.

[33] L. Dhar, L. Clapham, D.L. Atherton, “Influence of uniaxial plastic deformation on magnetic Barkhausen noise in steel,” *NDT&E Int.,* vol. 34, iss. 8, pp. 507 – 514, 2001.

[34] K. Li, L. Li, P. Wang, J. Liu, Y. Shi, Y. Zhen, S. Dong, “A fast and non-destructive method to evaluate yield strength of cold-rolled via incremental permeability,” *J. Magn. Magn. Mater.,* vol. 498, 166087, 2020.

[35] B. Gupta, T. Uchimoto, B. Ducharne, G. Sebald, T. Miyazaki, T. Takagi, “Magnetic incremental permeability non-destructive evaluation of 12 Cr-Mo-W-V steel creep test samples with varied ageing levels and thermal treatments,” *NDT&E Int.,* vol. 104, pp. 42 – 50, 2019.

[36] J.S. Urbach, R.C. Madison, J.T. Market, “Reproducibility of magnetic avalanches in an Fe-Ni-Co ferromagnet,” *Phys. Rev. Lett.,* vol. 75, 4694, 1995.

[37] J.R. Petta, M.B. Weissman, K. P. O'Brien, "Multiple magnetization paths in Barkhausen noise," *Phys. Rev. E,* vol. 54, R1029(R), 1996.

[38] J.R. Petta, M.B. Weissman, G. Durin, "Dependence of Barkhausen pattern reproducibility on hysteresis loop size," *Phys. Rev. E,* vol. 56, 2776, 1997.

[39] IEC 60404-3, "Magnetic materials – Part 3: Methods of measurement of the magnetic properties of electrical strip and sheet by means of a single sheet tested," International Electrotechnical Commission, 2010.

[40] B. Gupta, B. Ducharne, T. Uchimoto, G. Sebald, T. Miyazaki, T. Takagi, "Comparison of electromagnetic inspection methods for creep-degraded high chromium ferritic steels," *NDT&E Int.*, vol. 118, 102399, 2021.

[41] A. Yashan, G. Dobmann, "Measurements and semi-analytical modeling of incremental permeability using eddy current coil in the presence of magnetic hysteresis", in: F. Kojima, T. Takagi, S.S. Udpa, J. Pávó (Eds.), Electromagnetic Nondestructive Evaluation (VI), IOS press, pp. 150-157, 2002.

[42] P. Fagan, B. Ducharne, L. Daniel, A. Skarlatos, "Multiscale modelling of the magnetic Barkhausen noise energy cycles," *J. Magn. Magn. Mater.,* vol. 517, 167395, 2021.

[43] B. Gupta, B. Ducharne, T. Uchimoto, G. Sebald, T. Miyazaki, T. Takagi, "Non-destructive testing on creep degraded 12% Cr-Mo-W-V ferritic test samples using Barkhausen noise," *J. Magn. Magn. Mater.,* vol. 498, 166102, 2020.

[44] S. Zhang, B. Ducharne, S. Takeda, G. Sebald, T. Uchimoto, "Low-frequency behavior of laminated electric steel sheet: Investigation of ferromagnetic hysteresis loops and incremental permeability," *J. Magn. Magn. Mater.,* vol. 538, 168278, 2021.

[45] G. Bertotti, "General properties of power losses in soft ferromagnetic materials," *IEEE Trans. Magn.*, vol. 24, n° 1, pp. 621 – 630, 1988.

[46] IEC 60404-2, "Magnetic materials – Part 2: Methods of measurement of the magnetic properties of electrical steel strip and sheet by means of an Epstein frame," *International Electrotechnical Commission*, June 2008.

[47] IEC 60404-6, "Magnetic materials – Part 6: Methods of measurement of the magnetic properties of magnetically soft metallic and powder materials at frequencies in the range 20 Hz to 200 kHz by the use of ring specimens," *International Electrotechnical Commission*, June 2003.

[48] R. Valenzuela, I. Betancourt, "Giant magnetoimpedance, skin depth, and domain wall dynamics," *IEEE Trans. Mag.*, vol. 38, iss. 5, pp. 3081 – 3083, 2002.

[49] F. Qiu, M.J. Klug, G. Tian, P. Hu, J. McCord, “Influence of magnetic domain wall orientation on Barkhausen noise and magneto-mechanical behavior in electrical steel,” *J. Phys. D: App. Phys.*, vol. 52, 265001, 2019.

[50] M. Carara, M. N. Baibich, R. L. Sommer, “Magnetization dynamics as derived from magneto impedance measurements,” *J. App. Phys.*, vol. 88, n°1, pp. 331 – 335, 2000.

[51] S.E. Zirka, Y.I. Moroz, P. Marketos, A.J. Moses, “Viscosity-based magnetodynamic model of soft magnetic materials,” *IEEE Trans. Mag.*, vol. 42, n°9, pp. 2121 – 2132, 2006.

[52] M.A. Raulet, B. Ducharne, J.P. Masson, and G. Bayada, “The magnetic field diffusion equation including dynamic hysteresis: a linear formulation of the problem,” *IEEE Trans. Mag.,* Vol. 40, n° 2, pp. 872-875, 2004.

[53] M. Petrun, S. Steentjes, “Iron-loss and magnetization dynamics in non-oriented electrical steel: 1-D Excitations up to high frequencies,” *IEEE Access*, vol. 8, pp. 4568-4593, 2020.

[54] C. Appino, O. de la Barrière, F. Fiorillo, M. LoBue, F. Mazaleyrat, C. Ragusa, “Classical eddy current losses in soft magnetic composites,” *J. App. Phys.*, vol. 113, 17A322, 2013.

[55] T. Le Manh, F. Caleyo, J.M. Hallen, J.H. Espina-Hernández, J.A. Pérez-Benitez, “Model for the correlation between magnetocrystalline energy and Barkhausen noise in ferromagnetic materials,” *J. Magn. Magn. Mater.,* vol. 454, pp. 155 – 164, 2021.

[56] S.H.N. Kouakeuo, A. Solignac, R. Sabariego, L. Morel, M.A. Raulet, B. Toutsop, B. Tsafack, B. Ducharne, “Internal characterization of magnetic cores, comparison to finite element simulations: a route for dimensioning and condition monitoring,” *IEEE Trans. on Inst. and Meas., 6005310, 2022.*